metals

Article

In Situ Development and High Temperature Features of CoCrFeNi-M_6C_p High Entropy-Alloy Based Hardmetal

Huizhong Li [1,2,3], He Lin [1], Xiaopeng Liang [1,2,3,*], Weiwei He [4], Bin Liu [2], Yong Liu [2] and Li Wang [2,5,*]

[1] School of Materials Science and Engineering, Central South University, Changsha 410083, China; lhz606@csu.edu.cn (H.L.); hughlinhe@163.com (H.L.)
[2] State Key Laboratory of Powder Metallurgy, Central South University, Changsha 410083, China; binliu@csu.edu.cn (B.L.); yonliu@csu.edu.cn (Y.L.)
[3] Key Laboratory of Nonferrous Metal Materials Science and Engineering, Ministry of Education, Central South University, Changsha 410083, China
[4] Xi'an Sailong Metal Materials Co., Ltd., Xi'an 710016, China; hewi126@126.com
[5] Institute of Materials Research, Helmholtz-Zentrum Geesthacht, Max-Planck-Strasse 1, D-21502 Geesthacht, Germany
[*] Correspondence: liangxp@csu.edu.cn or mselxp@gmail.com (X.L.); Li.wang1@hzg.de (L.W.); Tel.: +86-731-8887794 (X.L.)

Received: 24 February 2020; Accepted: 17 March 2020; Published: 23 March 2020

Abstract: In this work, an in-situ CoCrFeNi-M_6C_p high entropy-alloy (HEA) based hardmetal with a composition of $Co_{25}Cr_{21}Fe_{18}Ni_{23}Mo_7Nb_3WC_2$ was fabricated by the powder metallurgy (PM) method. Microstructures and mechanical properties of this HEA were characterized and analyzed. The results exhibit that this HEA possesses a two-phase microstructure consisting of the face-centered cubic (FCC) matrix phase and the carbide M_6C phase. This HEA has an average grain size of 2.2 μm, and the mean size and volume fraction of carbide particles are 1.2 μm and 20%. The tensile tests show that the alloy has a yield strength of 573 MPa, ultimate tensile strength of 895 MPa and elongation of 5.5% at room temperature. The contributions from different strengthening mechanisms in this HEA were calculated. The grain boundary strengthening is the dominant strengthening mechanism, and the carbide particles are significant for the further enhancement of yield strength by the dislocation strengthening and Orowan strengthening. In addition, with increasing temperatures from 600 °C to 900 °C, the HEA shows a reduced yield strength (YS) from 473 MPa to 142 MPa, a decreased ultimate tensile strength (UTS) from 741 MPa to 165 MPa and an enhanced elongation from 10.5% to 31%.

Keywords: high entropy alloy; hardmetals; microstructure; tensile properties; strengthening mechanisms

---

1. Introduction

High entropy alloys (HEAs) have attracted significant research interests worldwide and shown potential application prospects in different fields due to their unique structure and properties [1–3]. HEAs are composed of at least four elements mixed in equiatomic or nearly equiatomic ratios and have a single-phase microstructure, possessing remarkable mechanical properties, high wear resistance, exceptional fatigue resistance, excellent corrosion resistance and high resistance to anneal softening [4–7]. Based on the phase constitution, HEAs can be divided into four types as follows: face-centered cubic (FCC) single-phase HEAs (e.g., CoCrFeNi and CoCrFeNiMn) [8–10], body-centered cubic (BCC) single-phase HEAs (e.g., TiNbTaZrAl, VNbMoTaW and HfNbTaTiZr) [11–13], hexagonal close-packed (HCP) single-phase HEAs (e.g., GdDyErHoTb and GdErHoTb) [14] and multiple-phase HEAs (e.g., AlCoCrFeNiCu, $AlCoCrFeNi_{2.1}$ and $CoCrFeNiMo_{0.5}W_{0.5}$) [15–17]. The microstructures and properties of these HEAs have been thoroughly investigated and reported. Previous studies [15–17] indicate that the HEA of mixing of the elements in a different atomic size tend to form intermetallic phases rather than a single solid solution phase. In addition, the metal-matrix composites were reported to have better mechanical properties due to the strengthening from the particle phase [18,19]. Therefore, it is attractive to design a HEA based hardmetal consisting of a HEA matrix phase and a second strengthening phase, which may have good mechanical properties.

It is reported that the FCC single-phase HEAs are ductile but not strong enough and the BCC single-phase HEAs are super strong but brittle [20]. The CoCrFeNi HEAs possess a single FCC phase resulting in a high elongation of 60% and a relatively low ultimate tensile strength (UTS) of 453 MPa [5]. Such superior ductility of the CoCrFeNi-based HEAs makes them become a hotspot for researchers to develop particle-reinforced HEAs in order to satisfy the structural applications [6,18,19]. In previous studies, the addition of Mo induced the precipitation of σ and μ intermetallic phases [21], Nb caused the formation of Laves phase [22,23], the combination of Mo and W or W induced the formation of δ-NiW and σ-CoCr phases [15] and carbides are favorable to form in HEAs with C addition or even no C content [18,19,24–26]. All these precipitated phases were reported to improve the strength of the CoCrFeNi-based HEAs. However, the studies on the simultaneous addition of Mo, Nb, W and C into the CoCrFeNi-based HEAs were scarcely reported. Moreover, compared to the literature on the mechanical properties of the CoCrFeNi-based HEAs at room temperature, the studies on the high temperature properties are relatively less [10,16–18,27–31]. The high temperature properties of the FCC-based HEAs were investigated in a different status, such as as-cast [26], rolled [27,28], different grain size [10,29,30] and multiple phases [16–18]. The ultrafine grain, rolled and multiple phases make the FCC-based HEAs possess higher room temperature mechanical properties (e.g., UTS is 995 MPa in Reference [30] and 1170 MPa in Reference [16]) but insufficient performances at elevated temperature, which the UTS is less than 600 MPa at 600 °C and basically less than 300 MPa at 800 °C. Therefore, the balance of the properties at room temperature and elevated temperature is in urgent need.

Generally, the HEAs fabricated by ingot metallurgy (IM) have a typical dendritic structure with coarse grains and serious segregation of interstitial elements [8,20]. Instead, powder metallurgy (PM) is an efficient method to produce multicomponent alloys with homogeneous elements distribution, which results in fine microstructures and admirable mechanical properties [8,9,32]. In this study, the powder metallurgy method was used to produce a two-phase CoCrFeNi HEA based hardmetal. The elements powders (Co, Cr, Fe, Ni, Mo, Nb, W and C) were firstly mechanically alloyed and subsequently consolidated by hot-pressing sintering. The tensile tests were carried out at different temperatures and the microstructures were characterized by a combination of X-ray diffraction (XRD), scanning electron microscopy (SEM), electron probe microanalysis (EPMA) and transmission electron microscopy (TEM) methods to thoroughly understand the HEA hardmetal.

2. Experimental

2.1. Material Preparation

The investigated high-entropy alloy (HEA) with a composition of $Co_{25}Cr_{21}Fe_{18}Ni_{23}Mo_{7}Nb_{3}WC_{2}$ (at.% throughout the paper) was prepared by powder metallurgy (PM). Element powders of Co, Cr, Fe, Ni, Mo, Nb, W and C with purity higher than 99.9 wt % and particle size less than 75 μm were firstly mechanically alloyed (MA) in a ball mill with stainless steel vial in argon atmosphere. The ball-to-powder ratio was 60:1 and the rotation speed of milling was 940 rpm during the milling process. Additionally, the milling was conducted for a total of 4 h, comprising of four cycles of 60 min of milling and 10 min idle time. Subsequently, the as-milled powders were consolidated by hot-pressing sintering (HPS) at a sintering temperature of 1100 °C and pressure of 30 MPa for 2 h. The heating rate was 10 °C /min.

2.2. Microstructural Characterization

The phase constitutions of the samples were identified by an X-ray diffractometer (XRD, D/Max 2500, Rigaku lnc., Tokyo, Japan) using Cu Kα radiation scanning from 20° to 100° at a step size of 0.02°. The microstructures and chemical compositions of phases were characterized by a scanning electron microscope (SEM, SIRION 200, FEI lnc., Hillsboro, OR, USA) equipped with an electron backscatter diffraction (EBSD) analyzer (XM4-Hikari, EDAX lnc., Mahwah, NJ, USA), an electron probe microanalyzer (EPMA, JXA-8230, JEOL Ltd., Tokyo, Japan) and a transmission electron microscope (TEM, Tecnai G^{2}20, FEI lnc., Hillsboro, OR, USA). SEM and EPMA specimens were mechanically ground with sand papers and then polished with diamond paste. The TEM slices were firstly ground to a thickness of about 50 μm and then thinned to electron transparency using a twin-jet electro-polishing machine with a solution of 5% perchloric acid and 95% alcohol at 25 V and −30 °C. The mean size and volume fraction of carbide particles was measured by using Image Pro Plus software (version 6, Media Cybernetics lnc., Rockville, MD, USA) based on multiple SEM images and a statistical average was taken.

2.3. Mechanical Property Characterization

Tensile tests were performed at an Instron 3369 testing machine (Instron Ltd., Norwood, MA, USA) equipped with a furnace for heating up to 1200 °C. The tests were conducted at room temperature and elevated temperatures in the range of 600–900 °C under an air atmosphere at a strain rate of 10^{-3} s^{-1}. The high temperature extensometer was used to measure the deformation of tensile tests at elevated temperatures. The specimens were prepared by electric discharge machining with a gauge length of 8 mm and a gauge cross-section of 3.5 mm × 2.5 mm. The surface of specimens was mechanically polished before tensile tests.

3. Results

3.1. Microstructure

The phase constitution of the HEA was analyzed by XRD as shown in Figure 1a. The alloy was composed of a face-centered cubic (FCC) structure matrix phase and a carbide phase M_6C. Additionally, the lattice parameters of the FCC matrix phase and the M_6C phase were 0.3601 nm and 1.1173 nm, respectively, which can be obtained from refined XRD patterns. By checking the SEM microstructure under back-scattered electron mode shown in Figure 1b, the FCC matrix phase exhibited a grey contrast while the carbide phase showed brightness. In addition, in order to confirm the structure of the phase constitutions of the HEA, further TEM investigation was conducted. Figure 1c revealed a TEM bright field (BF) image together with diffraction patterns recorded from the matrix and dark particle phase. By analyzing the diffraction patterns, the matrix phase had an FCC structure with lattice parameter a = 0.3593 nm and the particle phase was FCC-M_6C carbide with lattice parameter a = 1.1141 nm, which agreed with the XRD results. Figure 1d shows the size distribution of carbide particles in the HEA, which was measured by using Image Pro Plus software (version 6, Media Cybernetics lnc., Rockville, MD, USA) based on the bright phase of multiple SEM images (see supplementary data Figure S1). Additionally, the mean size and volume fraction of the carbide phase were measured as 1.2 μm and 20%, respectively. In addition, the inverse pole figure (IPF) plus image quality (IQ) image in Figure 1e display the grains having different orientations with different colors, and Figure 1f shows the profile of the grain size distribution with the mean grain diameter of 2.2 μm.

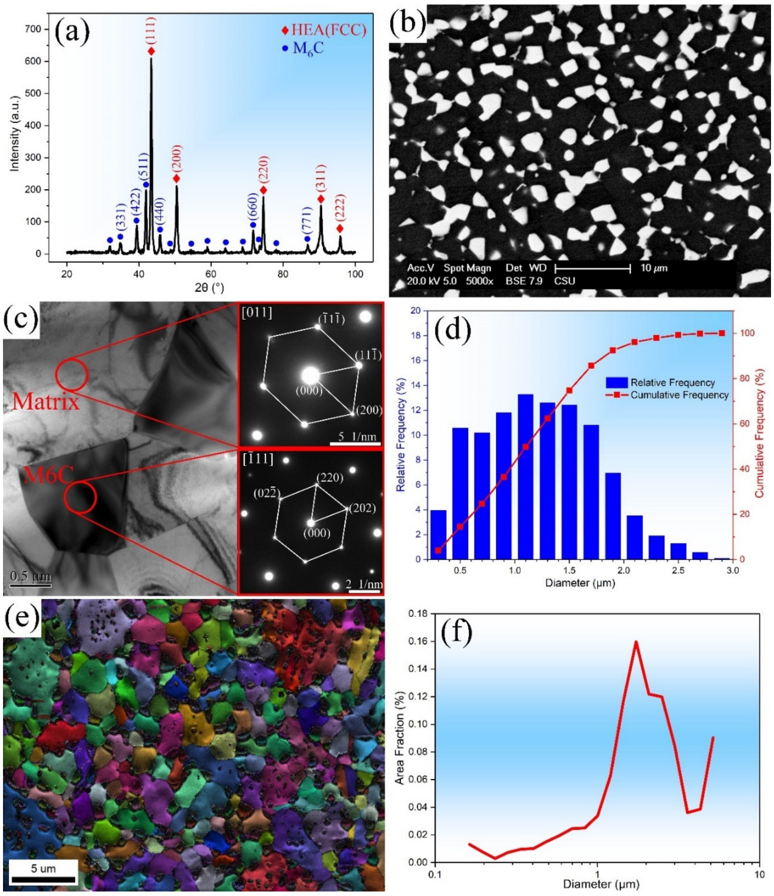

Figure 1. (**a**) XRD patterns of the high entropy alloy (HEA), (**b**) SEM micrograph of the HEA, (**c**) TEM image and selected area electron diffraction (SAED) patterns of the HEA, (**d**) size distribution of the carbide particles in the HEA, (**e**) IPF + IQ map and (**f**) grain size distribution of the HEA.

Figure 2 exhibits the line distributions of elements in the matrix phase and carbide phase of the HEA by EPMA. The matrix FCC phase (dark zones) is enriched in Co, Cr, Fe and Ni, and Mo, Nb, W and C were mainly distributed within the carbide phase (bright zones). Table 1 presents the chemical compositions of the two phases measured by EPMA. The FCC matrix phase has a composition consisted predominantly of Co, Cr, Fe and Ni with nearly equiatomic ratios and was depleted with Mo, Nb and W. While, the carbide phase was enriched in Mo, Nb and C. Additionally, the atomic ratio of C and other elements in the carbide was nearly 1:6, which indicates that the carbide phase was (Co, Cr, Fe, Ni, Mo, Nb, W)$_6$C (M$_6$C). The results were in good agreement with the XRD results shown in Figure 1a.

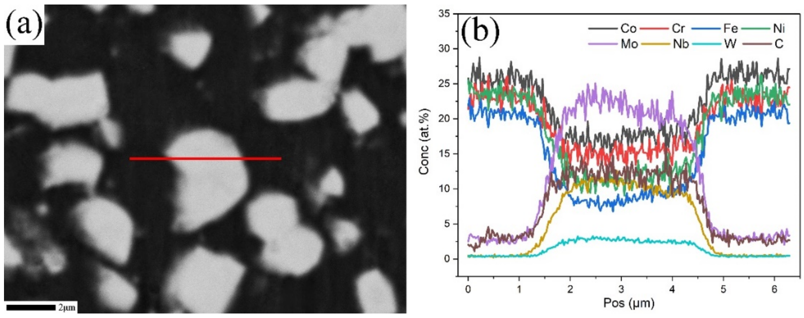

Figure 2. (**a**) Microstructure image and (**b**) the distributions of elements in matrix phase and carbide phase of the HEA by electron probe microanalyzer (EPMA).

Table 1. Chemical compositions of the two phases in the HEA by EPMA (at.%).

Elements	Co	Cr	Fe	Ni	Mo	Nb	W	C
Matrix	26.48	21.80	19.19	23.88	3.87	0.46	0.46	3.56
Carbide	15.17	14.53	6.71	11.68	22.33	11.84	2.94	14.38

3.2. Mechanical Properties

Figure 3a shows the engineering stress-strain curves of the HEA at different temperatures and strain rate of 10^{-3} s^{-1}, and Figure 3b revealed the profiles of the yield strength (YS), ultimate tensile strength (UTS) and elongation of the HEA as a function of testing temperatures. The HEA has a 0.2% offset yield strength (YS) of 573 MPa, an ultimate tensile strength (UTS) of 895 MPa and an elongation (EL) of 5.5% at room temperature. With the temperature increases from 600 °C to 900 °C, the YS decreased from 473 MPa to 142 MPa, the UTS decreased gradually from 741 MPa to 165 MPa and the elongation increased from 10.5% to 31%. The tensile curve still shows obvious work hardening behavior at 600 °C, which is shown as the difference between YS and UTS in Figure 3b. However, the difference between YS and UTS in Figure 3b reduced significantly as the test temperature increased, indicating that the work hardening reduced dramatically. As shown in Figure 3a, a weak work hardening was observed after the yield point at higher tested temperatures. Especially at 800–900 °C, the deformation behavior exhibited a steady-state after yielding, indicating that the work hardening and temperature softening achieved a state of equilibrium, which resulted in a better ductility. In addition, the hardness of the HEA was stable (320–330 HV) after holding at different temperatures for 4 h (see supplementary data Figure S2), which indicates that there was no heat treatment strengthening during tensile tests.

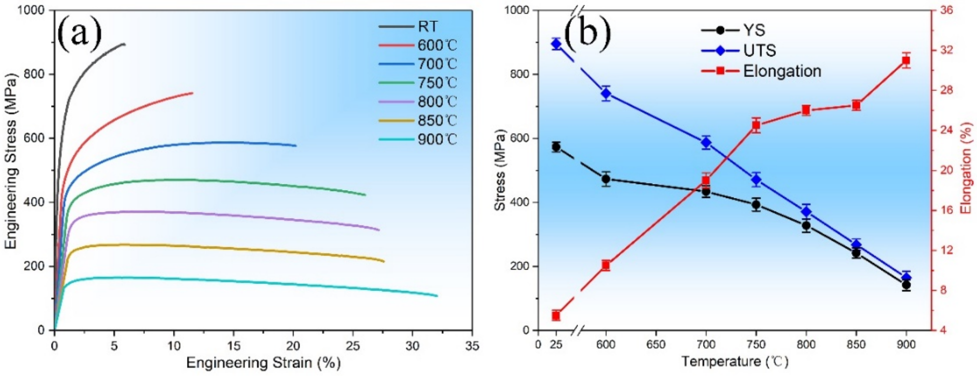

Figure 3. (**a**) Engineering stress-strain curves of the HEA at different temperatures, (**b**) temperature dependence of the yield strength (YS), ultimate tensile strength (UTS) and elongation of the HEA tested at a strain rate of 10^{-3} s^{-1}.

Figure 4 shows the fracture morphologies of the HEA after tensile tests at different temperatures. The morphology of the fracture surface in the specimen tested at room temperature in Figure 4a exhibited numerous flat facets united with each other by few tearing edges, indicating that the brittle fracture dominated. The flat facets were induced by the fracture of hard carbide while the tearing edges were caused by the deformation of the ductile matrix. Moreover, it should be noted that some intragranular cracks could be observed in the fracture surface. As the test temperature rose, the fracture surface shows increasing fine dimples indicating that the alloy becomes more ductile. The fracture surface of the HEA tested at 700 °C in Figure 4b shows flat facets and cracks, but with more tearing edges, indicating a much better ductility. The typical dimples morphology appeared in the sample after tested at 800 °C in Figure 4c and numerous dimples with plastic deformation can be observed in Figure 4d. The ductile matrix could do more plastic deformation at a higher temperature, meaning the more elongation as shown in Figure 3. Therefore, the hard carbides dominated the deformation at lower temperatures while the plastic deformation of the matrix was more favorable at higher temperatures, which results in the brittle fracture gradually converting to the ductile dimpled fracture as the tensile temperature increased.

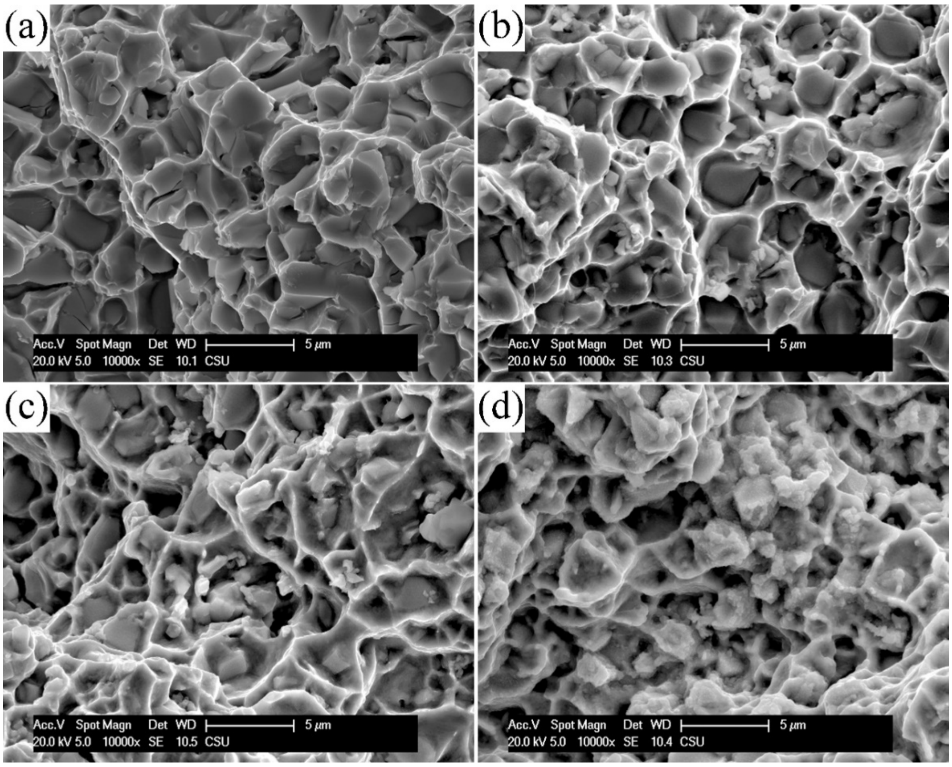

Figure 4. The fracture morphologies of the HEA after tensile tests at different temperatures. (**a**) Room temperature, (**b**) 700 °C, (**c**) 800 °C and (**d**) 900 °C.

Figure 5 displays the TEM microstructures of the HEA after tensile tests at different temperatures. The TEM image in Figure 5a shows the microstructure of the sample after being tested at room temperature, the density of dislocation significantly increased due to the severe deformation. Strong dislocation/dislocation interactions were observed in the matrix, which further hindered the glide of dislocations. Additionally, numerous dislocations clustered around the carbide particles, indicating that the carbide particles inhibited the movements of dislocations. These together contributed to a high ultimate strength of 895 MPa for the HEA at room temperature. When the HEA samples were conducted at tensile tests at elevated temperatures, the dislocations with a lower density could be observed. In Figure 5b, the accumulation of dislocations at grain boundaries revealed that the movement of dislocations was hindered by grain boundaries and M_6C particles. Additionally, the dislocations became rare in the sample after being tested at 900 °C (Figure 5d), indicating that the dislocation annihilation was more advantageous at higher temperatures. In addition, no obvious deformation and solid solution of the M_6C particles and no precipitations in the matrix phases were observed after being tested at elevated temperatures, showing that the matrix and M_6C particles possessed a high thermal stability during the elevated temperature tensile tests. Therefore, M_6C hindering the movements of dislocations and grain boundaries played a role in hardening, while the dislocation annihilation played a role in softening during the deformation at elevated temperatures.

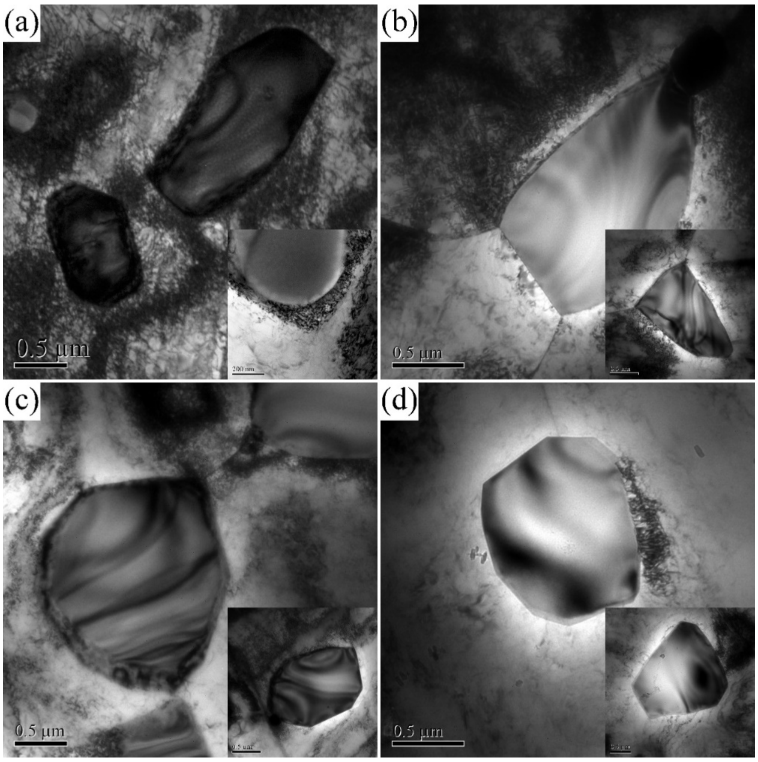

Figure 5. The TEM microstructures of the HEA after tensile tests at different temperatures. (**a**) Room temperature, (**b**) 700 °C, (**c**) 800 °C and (**d**) 900 °C.

4. Discussion

The results presented in this study revealed that a two-phase structure composed of an FCC phase and a carbide phase could be obtained in the CoCrFeNi-based HEA added with the refractory elements Mo, Nb, W and C. The carbide particles were advantageous for improving the mechanical properties (YS of 573 MPa and UTS of 895 MPa) of the HEA. This is because the motion of dislocations and grain boundaries in the deformation process will be restrained by the carbide particles.

To explore the strengthening mechanisms in this HEA hardmetal, the yield strength can be written in the following equation, which is the sum of the matrix strength σ_m and the reinforcement from the particles σ_p:

$$\sigma_y = \sigma_m + \sigma_p \tag{1}$$

The σ_m contains the frictional stress σ_a and grain boundary strengthening σ_g. The frictional stress σ_a is the lattice resistance to dislocation motion in single-phase alloys, which is the yield strength of CoCrFeNi HEAs. According to the data in References [33,34], the rule of the mixture analysis was applied to estimate the frictional stress of this CoCrFeNi-based matrix, which is calculated as 146 MPa. Compared with other studies, the strength is about 147 MPa [22], 155 MPa [21] and 165 MPa [5], so the estimated value is reasonable.

According to the Hall-Petch equation, the grain boundaries strengthening can be expressed as [32,35]:

$$\sigma_g = K_{HP} \times d^{-1/2} \tag{2}$$

where K_{HP} stands for the Hall-Petch constant and d (about 2.2 μm) is the average grain size. As discussed in Reference [33], the value of K_{HP} can be assumed as 447 MPa·μm$^{1/2}$ in the studied HEA. Consequently, the value of σ_g is estimated as 301 MPa. It demonstrates that the fine structure is much more effective on the strengthening in the HEAs. Additionally, the matrix strength σ_m can be calculate as 447 MPa combining the value of σ_a and σ_g.

In the HEA, in-situ M_6C particles leads to the good bonding between the matrix and particles, increasing the strength by the load transfer from the matrix to particles. In addition, the dislocations will generate due to the lattice strain caused by the different coefficient of thermal expansion and the elastic moduli between the matrix and particles during the cooling process, and the particles will further impede the dislocations motion. Therefore, the reinforcement of particles can be expressed as [36]:

$$\sigma_p = \sigma_l + \sigma_d + \sigma_o \tag{3}$$

where σ_l is load bearing effect, σ_d is dislocation strengthening or strain strengthening and σ_o is the Orowan strengthening (the dislocations will pass by the precipitates when the particle size is large in the matrix).

The load bearing effect σ_l is presented as [35]:

$$\sigma_l = 0.5f\sigma_a \tag{4}$$

where f is the volume fraction of carbide particles with a value of 20% and σ_a is the stress of matrix. Hence, we calculated σ_l = 15 MPa.

The dislocation strengthening σ_d can be described as following using a Bailey-Hirsch formula [37]:

$$\sigma_d = M\alpha G_M b\sqrt{\rho} \tag{5}$$

where M is the Taylor factor converting shear stress to normal stress for FCC polycrystalline matrix and has a value of 3.06, $\alpha = 0.2$ is a constant for FCC materials [5] and G_M is the shear modulus for CoCrFeNi-based matrix [38]. b is the magnitude of the Burger vector and $b = a/\sqrt{2}$ (a is the lattice constant) for the FCC structure. ϱ is the initial dislocation density, and can be calculated from $\rho = \frac{2\sqrt{3}\delta}{db}$ [39,40], where d is grain size and δ is micro-strain. The XRD peak broadening consists of the grain size broadening and the micro strain broadening, so we can estimate the δ by the equation of $\Delta\theta \cdot \cos\theta = \frac{K\lambda}{d} + 4\delta \cdot \sin\theta$ [5,41], where $\Delta\theta$ is full width at half maximum in the XRD pattern after subtracting the instrumental broadening, K is a constant of 0.9, λ = 0.154056 nm is the wavelength of Cu Kα radiation, d is grain size and θ is the Bragg angle of the corresponding peaks. We took the average value of δ = 0.002 based on peaks of the matrix, so ϱ can be properly estimated as 1.24×10^{13} m^{-2} and the dislocation strengthening σ_d = 46 MPa.

In this work, the Ashby-Orowan equation is applicable to estimate the Orowan strengthening [42],

$$\sigma_o = \frac{0.13G_M b}{D\left[(1/2f)^{1/3} - 1\right]} \ln\left(\frac{D}{2b}\right) \tag{6}$$

where f = 20% is the volume fraction and D = 1.2 µm is the spatial diameter of carbide particles (the carbide particles are simply considered as sphere). Hence, the increments of Orowan strengthening can be evaluated as 50 MPa. Additionally, the yield strength improvement from particles σ_p was calculated as 111 MPa from Equation (4).

As discussed above, the calculated value of matrix strength was 447 MPa, which the contribution from grain boundary strengthening was the dominant strengthening mechanism in the HEA. In addition, the value of reinforcement from particles was 111 MPa, indicating that the generation of carbide particles had a significant effect on the enhancement of the yield strength in the HEA by dislocation strengthening and Orowan strengthening. The calculated yield strength was 558 MPa, which is a little lower than the measured yield strength of 573 MPa. The deviation may be attributed to the approximate parameters cited from other HEAs and the irregular particles considered as spherical particles. In general, the calculated yield strength was consistent with the measured data, and the current HEA shows outstanding mechanical properties on account of the multiple strengthening mechanisms, especially the grain boundary strengthening.

Figure 6 compares the tensile properties at room temperature and at elevated temperatures of the investigated HEA in this study with those of other FCC-based HEAs reported in the literature. Figure 6a shows the UTS and elongation at room temperature of different CoCrFeNi-based HEAs [5,8,21,22,43,44]. The CoCrFeNi HEAs in the literature were reported to have low UTS (400–500 MPa for as-cast HEAs [5,21,22,42] and 700–800 MPa for PM HEAs [8,42]) and high elongation (40–70%). With the addition of a small amount of Mo (2–7%), Nb (2.5–4%) and C (1.2%) in to the CoCrFeNi system, the UTS could be greatly improved but with an obvious decline in ductility. In this work, the CoCrFeNi-based HEA added with all Mo, Nb, W and C shows a higher UTS due to the reinforcement of M_6C. Figure 6b displays the profiles of the UTS of the FCC-based HEAs as a function of testing temperatures. The rolled CoCrFeNiMn HEAs [27,28] have higher UTS at room and elevated temperature than the as-cast CoCrFeNiMn HEA [26], and the fine microstructure with a different grain size also has a great impact on the performance of HEAs [10,29]. Jeong et al. [31] reported the $Fe_{41}Mn_{25}Ni_{24}Co_8Cr_2$ HEA (FCC) with an ultrafine grain size (≤0.5 μm) exhibited outstanding UTS (995 MPa) at room temperature but the UTS sharply dropped (less than 200 MPa) above 700 °C due to coarse grains after recrystallization. In addition, the UTS at a room temperature of FCC-based HEAs can be remarkably improved due to strengthening effects from other phases [16,18]. The forged AlCrCuNiFeCo HEA [16] with a microstructure consisting of FCC, BCC and σ phases showed a high UTS of 1170 MPa at room temperature but the UTS was very low above 700 °C (less than 100 MPa) because of the brittle to ductile transition. Compared to other FCC-based HEAs in Figure 6b, the HEA in this work exhibited a superior UTS, especially at elevated temperatures. It is reported that carbide M_6C shows a high thermal stability at the tested elevated temperatures in our work [45–47], which is proved in the TEM observations in Figure 5. Additionally, the movement of grain boundaries is important for the deformation at elevated temperatures, but the M_6C particles at grain boundaries will hinder the movements, which further slows down the coarsening rate of the matrix grains [46]. Therefore, the M_6C particles still exhibits a significant strengthening effect in the CoCrFeNi-based HEA at elevated temperature, which is very useful when the present HEA hardmetal is applied as a high-temperature structural material.

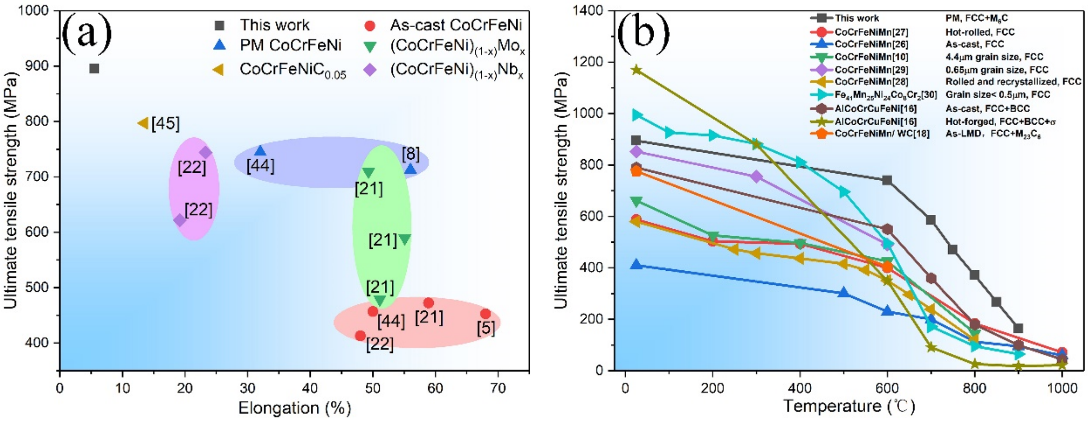

Figure 6. (**a**) Room-temperature tensile properties and (**b**) temperature dependence of the UTS of the HEA in this work and other FCC-based HEAs reported in literature.

5. Conclusions

(1) The HEA hardmetal fabricated by PM has a two-phase microstructure consisting of the CoCrFeNi-based FCC matrix and the carbide phase M_6C. Additionally, the average grain diameter was 2.2 μm, the mean size and volume fraction of carbide particles were 1.2 μm and 20%.

(2) The HEA hardmetal had a yield strength of 573 MPa, ultimate tensile strength of 895 MPa and elongation of 5.5% at room temperature.

(3) The contributions to the alloy strength from different strengthening mechanisms were quantitatively evaluated and the contribution from the grain boundary strengthening was the most

important. M_6C particles were important for the further enhancement of yield strength by the dislocation strengthening and Orowan strengthening.

(4) The HEA hardmetal shows a reduced yield strength from 473 MPa to 142 MPa, a decreased ultimate tensile strength from 741 MPa to 165 MPa and an enhanced elongation from 10.5% to 31% with increasing temperature from 600 °C to 900 °C. The work hardening reduced as the tested temperature increased. Additionally, the deformation behavior shows a steady-state after yielding at 800 °C to 900 °C.

(5) The M_6C particles still show a significant role in hardening at elevated temperatures by hindering the movements of dislocations and grain boundaries.

Supplementary Materials: The following are available online at http://www.mdpi.com/2075-4701/10/3/408/s1, Figure S1: SEM images of the HEA for calculating the mean size and volume fraction of carbides by using Image Pro Plus, Figure S2: Hardness of the HEA after heat treatment at different temperatures for 4 h.

Author Contributions: Conceptualization, H.L. (Huizhong Li); Data curation, H.L. (He Lin); Formal analysis, H.L. (Huizhong Li), Y.L. and L.W.; Funding acquisition, B.L.; Investigation, H.L. (He Lin); Methodology, H.L. (Huizhong Li); Project administration, X.L.; Resources, W.H.; Supervision, X.L.; Validation, H.L. (He Lin) and W.H.; Writing—original draft, H.L. (He Lin); Writing—review and editing, H.L. (Huizhong Li), X.L. and L.W. All authors have read and agreed to the published version of the manuscript.

Funding: This research was funded by National Natural Science Foundation of China, grant number 51671217 and 51771232, National Natural Science Funds for Distinguished Young Scholar of China, grant number 51625404, National key research and development plan of China, grant number 2016YFB0700302 and Fundamental Research Fund for the Central Universities of Central South University, grant number 502041002.

Conflicts of Interest: The authors declare no conflict of interest.

References

1. Zherebtsov, S.; Stepanov, N.; Ivanisenko, Y.; Shaysultanov, D.; Yurchenko, N.; Klimova, M.; Salishchev, G. Evolution of Microstructure and Mechanical Properties of a CoCrFeMnNi High-Entropy Alloy during High-Pressure Torsion at Room and Cryogenic Temperatures. *Metals* **2018**, *8*, 123. [CrossRef]
2. Lopes, J.G.; Oliveira, J.P. A Short Review on Welding and Joining of High Entropy Alloys. *Metals* **2020**, *10*, 212. [CrossRef]
3. Haase, C.; Mora, L.A.B. From High-Manganese Steels to Advanced High-Entropy Alloys. *Metals* **2019**, *9*, 726. [CrossRef]
4. Poletti, M.G.; Fiore, G.; Gili, F.; Mangherini, D.; Battezzati, L. Development of a new high entropy alloy for wear resistance: $FeCoCrNiW_{0.3}$ and $FeCoCrNiW_{0.3}$+5 at.% of C. *Mater. Des.* **2017**, *115*, 247–254. [CrossRef]
5. He, J.Y.; Wang, H.; Huang, H.L.; Xu, X.D.; Chen, M.W.; Wu, Y.; Liu, X.J.; Nieh, T.G.; An, K.; Lu, Z.P. A precipitation-hardened high-entropy alloy with outstanding tensile properties. *Acta Mater.* **2016**, *102*, 187–196. [CrossRef]
6. Shi, Y.Z.; Bin Yang, B.; Liaw, P.K. Corrosion-Resistant High-Entropy Alloys: A Review. *Metals* **2017**, *7*, 43. [CrossRef]
7. Jiang, H.; Qiao, D.X.; Lu, Y.P.; Ren, Z.; Cao, Z.Q.; Wang, T.M.; Li, T.J. Direct solidification of bulk ultrafine-microstructure eutectic high-entropy alloys with outstanding thermal stability. *Scr. Mater.* **2019**, *165*, 145–149. [CrossRef]
8. Liu, B.; Wang, J.S.; Liu, Y.; Fang, Q.H.; Wu, Y.; Chen, S.Q.; Liu, C.T. Microstructure and mechanical properties of equimolar FeCoCrNi high entropy alloy prepared via powder extrusion. *Intermetallics* **2016**, *75*, 25–30. [CrossRef]
9. Liu, Y.; Wang, J.S.; Fang, Q.H.; Liu, B.; Wu, Y.; Chen, S.Q. Preparation of superfine-grained high entropy alloy by spark plasma sintering gas atomized powder. *Intermetallics* **2016**, *68*, 16–22. [CrossRef]
10. Otto, F.; Dlouhý, A.; Somsen, C.; Bei, H.; Eggeler, G.; George, E.P. The influences of temperature and microstructure on the tensile properties of a CoCrFeMnNi high-entropy alloy. *Acta Mater.* **2013**, *61*, 5743–5755. [CrossRef]
11. Cao, Y.K.; Liu, Y.; Liu, B.; Zhang, W.D. Precipitation behavior during hot deformation of powder metallurgy Ti-Nb-Ta-Zr-Al high entropy alloys. *Intermetallics* **2018**, *100*, 95–103. [CrossRef]

12. Lee, W.H.; Park, K.B.; Yi, K.W.; Lee, S.Y.; Park, K.; Lee, T.W.; Na, T.W.; Park, H.K. Synthesis of Spherical V-Nb-Mo-Ta-W High-Entropy Alloy Powder Using Hydrogen Embrittlement and Spheroidization by Thermal Plasma. *Metals* **2019**, *9*, 1296. [CrossRef]
13. Eleti, R.R.; Bhattacharjee, T.; Shibata, A.; Tsuji, N. Unique deformation behavior and microstructure evolution in high temperature processing of HfNbTaTiZr refractory high entropy alloy. *Acta Mater.* **2019**, *171*, 132–145. [CrossRef]
14. Yuan, Y.; Wu, Y.; Tong, X.; Zhang, H.; Wang, H.; Liu, X.J.; Ma, L.; Suo, H.L.; Lu, Z.P. Rare-earth high-entropy alloys with giant magnetocaloric effect. *Acta Mater.* **2017**, *125*, 481–489. [CrossRef]
15. Shang, C.Y.; Axinte, E.; Sun, J.; Li, X.T.; Li, P.; Du, J.W.; Qiao, P.C.; Wang, Y. CoCrFeNi ($W_{1-x}Mo_x$) high-entropy alloy coatings with excellent mechanical properties and corrosion resistance prepared by mechanical alloying and hot pressing sintering. *Mater. Des.* **2017**, *117*, 193–202. [CrossRef]
16. Kuznetsov, A.V.; Shaysultanov, D.G.; Stepanov, N.D.; Salishchev, G.A.; Senkov, O.N. Tensile properties of an AlCrCuNiFeCo high-entropy alloy in as-cast and wrought conditions. *Mater. Sci. Eng. A* **2012**, *533*, 107–118. [CrossRef]
17. Zhang, Y.L.; Wang, X.G.; Li, J.G.; Huang, Y.Q.; Lu, Y.P.; Sun, X.F. Deformation mechanism during high-temperature tensile test in an eutectic high-entropy alloy $AlCoCrFeNi_{2.1}$. *Mater. Sci. Eng. A* **2018**, *724*, 148–155. [CrossRef]
18. Li, J.F.; Xiang, S.; Luan, H.W.; Amar, A.; Liu, X.; Lu, S.Y.; Zeng, Y.Y.; Le, G.M.; Wang, X.Y.; Qu, F.S.; et al. Additive manufacturing of high-strength CrMnFeCoNi high-entropy alloys-based composites with WC addition. *J. Mater. Sci. Technol.* **2019**, *35*, 2430–2434. [CrossRef]
19. Zhou, R.; Chen, G.; Liu, B.; Wang, J.W.; Han, L.L.; Liu, Y. Microstructures and wear behaviour of $(FeCoCrNi)_{1-x}(WC)_x$ high entropy alloy composites. *Int. J. Refract. Met. Hard Mater.* **2018**, *75*, 56–62. [CrossRef]
20. Lu, Y.P.; Dong, Y.; Guo, S.; Jiang, L.; Kang, H.J.; Wang, T.M.; Wen, B.; Wang, Z.J.; Jie, J.C.; Cao, Z.Q.; et al. A promising new class of high-temperature alloys: Eutectic high-entropy alloys. *Sci. Rep.* **2014**, *4*, 6200. [CrossRef]
21. Liu, W.H.; Lu, Z.P.; He, J.Y.; Luan, J.H.; Wang, Z.J.; Liu, B.; Liu, Y.; Chen, M.W.; Liu, C.T. Ductile $CoCrFeNiMo_x$ high entropy alloys strengthened by hard intermetallic phases. *Acta Mater.* **2016**, *116*, 332–342. [CrossRef]
22. Liu, W.H.; He, J.Y.; Huang, H.L.; Wang, H.; Lu, Z.P.; Liu, C.T. Effects of Nb additions on the microstructure and mechanical property of CoCrFeNi high-entropy alloys. *Intermetallics* **2015**, *60*, 1–8. [CrossRef]
23. He, F.; Wang, Z.J.; Cheng, P.; Wang, Q.; Li, J.J.; Dang, Y.Y.; Wang, J.C.; Liu, C.T. Designing eutectic high entropy alloys of $CoCrFeNiNb_x$. *J. Alloy. Comp.* **2016**, *656*, 284–289. [CrossRef]
24. Chen, J.; Yao, Z.H.; Wang, X.B.; Lu, Y.K.; Wang, X.H.; Liu, Y.; Fan, X.H. Effect of C content on microstructure and tensile properties of as-cast CoCrFeMnNi high entropy alloy. *Mater. Chem. Phys.* **2018**, *210*, 136–145. [CrossRef]
25. An, Q.; Wang, J.W.; Liu, Y.; Liu, B.; Guo, W.M.; Fang, Q.H.; Nie, Y. Effects of C and Mo on microstructures and mechanical properties of dual-phase high entropy alloys. *Intermetallics* **2019**, *110*, 106471. [CrossRef]
26. Gouvea, L.M.; Moravcik, I.; Omasta, M.; Veselý, J.; Cizek, J.; Minárik, P.; Cupera, J.; Záděra, A.; Jan, V.; Dlouhy, I. High-strength Al0.2Co1.5CrFeNi1.5Ti high-entropy alloy produced by powder metallurgy and casting: A comparison of microstructures, mechanical and tribological properties. *Mater. Charact.* **2020**, *159*, 110046. [CrossRef]
27. Kim, J.H.; Lim, K.R.; Won, J.W.; Na, Y.S.; Kim, H.S. Mechanical properties and deformation twinning behavior of as-cast CoCrFeMnNi high-entropy alloy at low and high temperatures. *Mater. Sci. Eng. A* **2018**, *712*, 108–113. [CrossRef]
28. Gali, A.; George, E.P. Tensile properties of high- and medium-entropy alloys. *Intermetallics* **2013**, *39*, 74–78. [CrossRef]
29. Fu, J.X.; Cao, C.M.; Tong, W.; Hao, Y.X.; Peng, L.M. The tensile properties and serrated flow behavior of a thermomechanically treated CoCrFeNiMn high-entropy alloy. *Mater. Sci. Eng. A* **2017**, *690*, 418–426. [CrossRef]
30. Sun, S.J.; Tian, Y.Z.; Lin, H.R.; Dong, X.G.; Wang, Y.H.; Wang, Z.J.; Zhang, Z.F. Temperature dependence of the Hall–Petch relationship in CoCrFeMnNi high-entropy alloy. *J. Alloy. Comp.* **2019**, *806*, 992–998. [CrossRef]

31. Jeong, H.T.; Kim, W.J. Grain size and temperature effect on the tensile behavior and deformation mechanisms of non-equiatomic Fe41Mn25Ni24Co8Cr2 high entropy alloy. *J. Mater. Sci. Technol.* **2020**, *42*, 190–202. [CrossRef]
32. Chlup, Z.; Fintová, S.; Hadraba, H.; Kuběna, I.; Vilémová, M.; Matějíček, J. Fatigue Behaviour and Crack Initiation in CoCrFeNiMn High-Entropy Alloy Processed by Powder Metallurgy. *Metals* **2019**, *9*, 1110. [CrossRef]
33. Wang, J.W.; Liu, B.; Liu, C.T.; Liu, Y. Strengthening mechanism in a high-strength carbon-containing powder metallurgical high entropy alloy. *Intermetallics* **2018**, *102*, 58–64. [CrossRef]
34. Sriharitha, R.; Murty, B.S.; Kottada, R.S. Alloying, thermal stability and strengthening in spark plasma sintered $Al_xCoCrCuFeNi$ high entropy alloys. *J. Alloy. Comp.* **2014**, *583*, 419–426. [CrossRef]
35. Liu, W.H.; Wu, Y.; He, J.Y.; Nieh, T.G.; Lu, Z.P. Grain growth and the Hall-Petch relationship in a high-entropy FeCrNiCoMn alloy. *Scr. Mater.* **2013**, *68*, 526–529. [CrossRef]
36. Habibnejad-Korayem, M.; Mahmudi, R.; Poole, W.J. Enhanced properties of Mg-based nano-composites reinforced with Al2O3 nano-particles. *Mater. Sci. Eng. A* **2009**, *519*, 198–203. [CrossRef]
37. Courtney, T.H. *Mechanical Behavior of Materials*, 2nd ed.; Waveland Press: Long Grove, IL, USA, 2005; pp. 179–181.
38. Wu, Z.; Bei, H.; Pharr, G.M.; George, E.P. Temperature dependence of the mechanical properties of equiatomic solid solution alloys with face-centered cubic crystal structures. *Acta Mater.* **2014**, *81*, 428–441. [CrossRef]
39. Ganji, R.S.; Karthik, P.S.; Rao, K.B.S.; Rajulapati, K.V. Strengthening mechanisms in equiatomic ultrafine grained AlCoCrCuFeNi high-entropy alloy studied by micro-and nanoindentation methods. *Acta Mater.* **2017**, *125*, 58–68. [CrossRef]
40. Williamson, G.K.; Smallman, R.E. Dislocation densities in some annealed and cold-worked metals from measurements on the X-ray debye-scherrer spectrum. *Philos. Mag.* **1956**, *1*, 34–46. [CrossRef]
41. Karolus, M.; Łągiewka, E. Crystallite size and lattice strain in nanocrystalline Ni-Mo alloys studied by Rietveld refinement. *J. Alloy. Comp.* **2004**, *367*, 235–238. [CrossRef]
42. Zhang, Z.; Chen, D.L. Consideration of Orowan strengthening effect in particulate-reinforced metal matrix nanocomposites: A model for predicting their yield strength. *Scr. Mater.* **2006**, *54*, 1321–1326. [CrossRef]
43. Brif, Y.; Thomas, M.; Todd, I. The use of high-entropy alloys in additive manufacturing. *Scr. Mater.* **2015**, *99*, 93–96. [CrossRef]
44. Zhou, R.; Liu, Y.; Zhou, C.S.; Li, S.Q.; Wu, W.Q.; Song, M.; Liu, B.; Liang, X.P.; Liaw, P.K. Microstructures and mechanical properties of C-containing FeCoCrNi high-entropy alloy fabricated by selective laser melting. *Intermetallics* **2018**, *94*, 165–171. [CrossRef]
45. Xu, Z.F.; Jiang, L.; Dong, J.S.; Li, Z.J.; Zhou, X.T. The effect of silicon on precipitation and decomposition behaviors of M6C carbide in a Ni–Mo–Cr superalloy. *J. Alloys Comp.* **2015**, *620*, 197–203. [CrossRef]
46. Li, J.R.; He, T.; Cheng, L.J.; Zhang, P.F.; Wang, L.W. Effect of precipitates on the hot embrittlement of 11Cr–3Co–3W martensitic heat resistant steel for turbine high temperature stage blades in ultra-supercritical power plants. *Mater. Sci. Eng. A* **2019**, *763*, 138187. [CrossRef]
47. Yu, K.; Shi, X.W.; Jiang, Z.G.; Li, C.W.; Chen, S.J.; Tao, W.; Zhou, X.T.; Li, Z.J. Effects of solution treatment on grain coarsening and hardness of laser welds in UNS N10003 alloy contained different carbon content. *J. Mater. Sci. Technol.* **2019**, *35*, 1719–1726. [CrossRef]